Electronic Supplementary Information

Naturally Derived Porous Carbon with Selective Metal- and/or Nitrogen- Doping for Efficient CO_2 Capture and Oxygen Reduction

Bingjun Zhu,[a] Kaipei Qiu,[a] Congxiao Shang[b] and Zhengxiao Guo[a]*

1. Sodium XPS high resolution scan

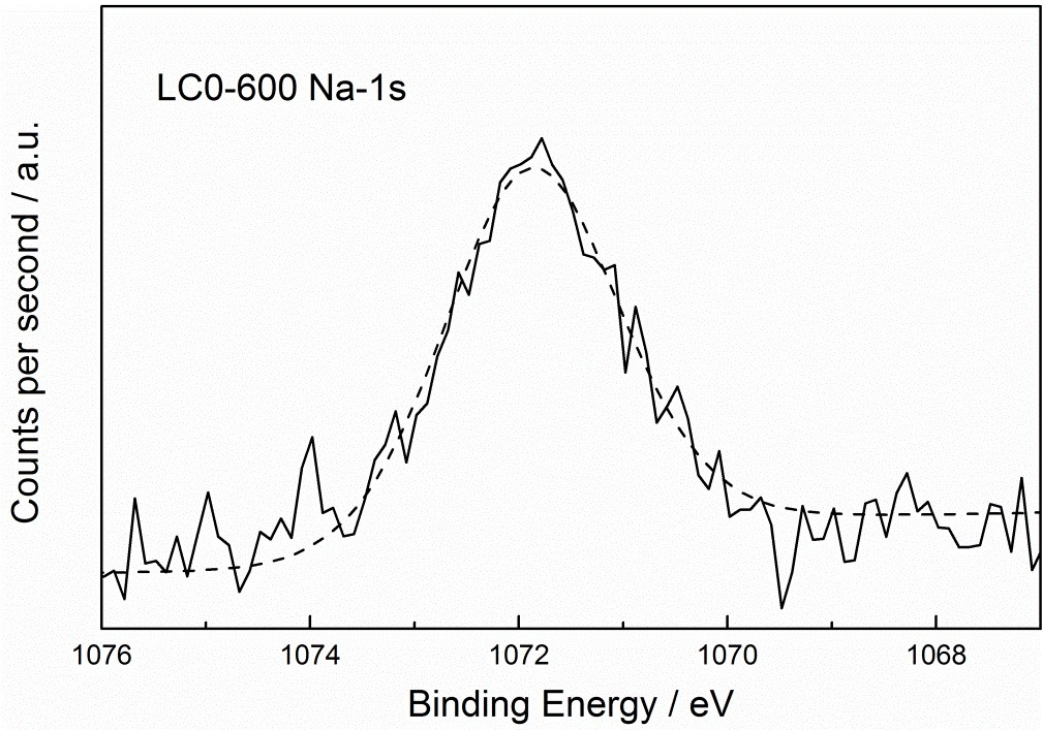

Figure S1 High resolution XPS Na-1s spectrum. It shows a single peak near 1072 eV, indicating Na exists in the form of +1 cations.

2. Micropore size distribution

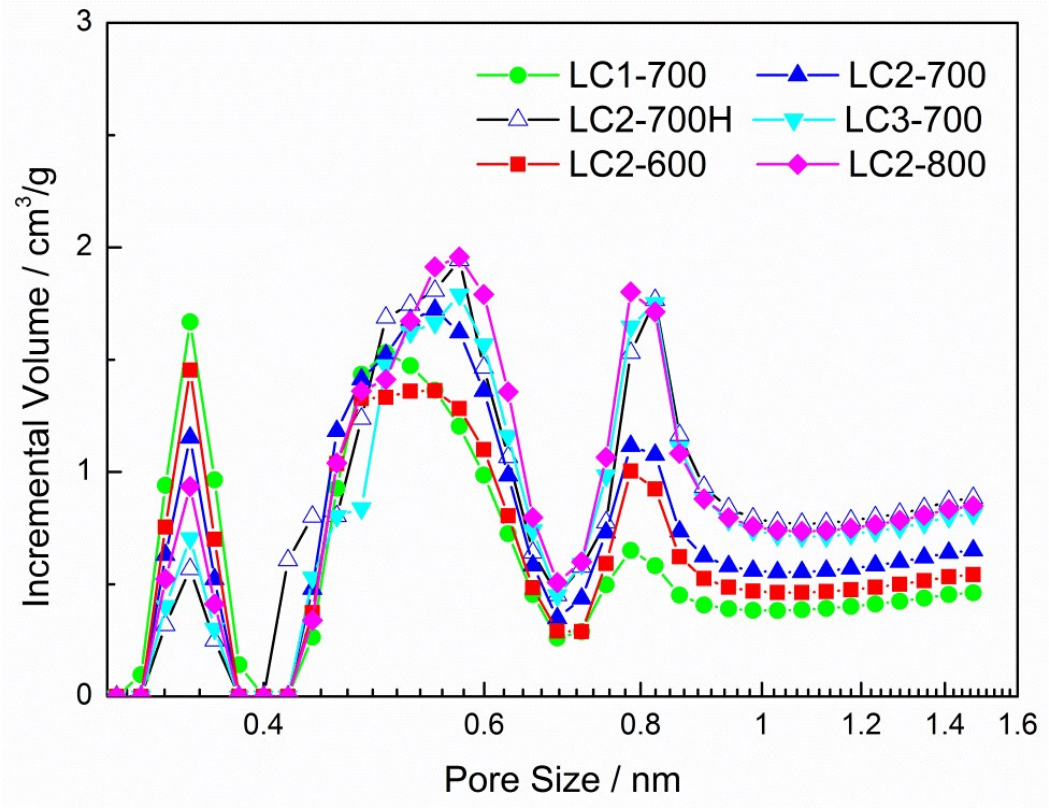

Figure S2: Micropore size distribution of leaf-derived carbon, determined by the 0 °C CO_2 adsorption isotherms.

3. BET and DFT surface area

Table S1: Comparison between specific surface area calculated by BET equation and NLDFT methods.

Sample	LC1-700	LC2-700	LC2-700H	LC3-700	LC2-600	LC2-800
S_{BET}	1080	1460	1510	2360	1050	1940
S_{DFT}	1360	1600	1630	2230	1210	1950

Table S1 is the comparison of specific surface area calculated by both BET equation and NLDFT methods. The specific surface area is frequently calculated by BET equation in the literature. However, Table 1 clearly shows there are differences between those results. BET method can either underestimate or overestimate the specific surface area of a sample. The underestimation is due to extreme curvature of ultramicropores (<0.7nm) and the relatively large size of the probe molecule (N_2). The overestimation is caused by the filling of probe molecules in the centre of the supermicrpore (>0.7nm). NLDFT gives a more realistic approach to describe the filling of probe molecules in micropores. The author recalculates the specific surface area of our samples by BET equation, in order to compare with those from the literature. BET surface area is used for the discussion in "Heat of Adsorption and Influence of Dopants" in the main manuscript.

4. Further analysis on heats of adsorption

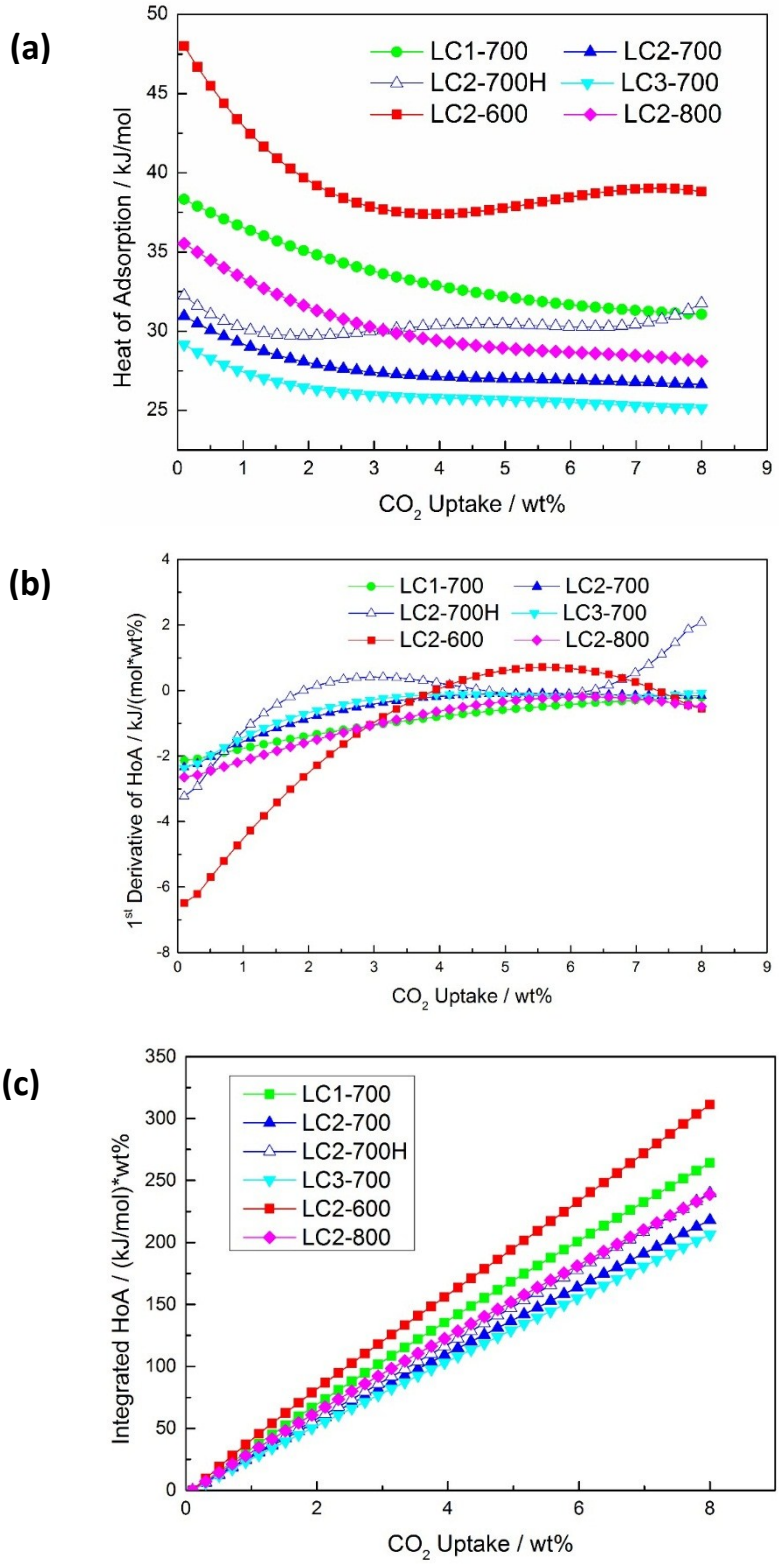

Figure S3: (a) Polynomial fitted heat of adsorption (HoA) plot and its corresponding (b) 1st order derivative and (c) integrated plots.

Figure S3a is the 4th order polynomial fitting of heat of adsorption between 0.1 and 8 wt% CO_2 uptakes. The fitting

process basically reproduces the shapes of curves plotted with experimental data points and also helps to predict heat of adsorption at even lower CO_2 uptakes. The fitted curve in Figure S3a is used to produce 1st order derivative and integrated heat of adsorption plots, which are shown in Figure S3b and c, respectively.

The 1st order derivative plot is an indication of how fast the heat of adsorption reduces with the increasing CO_2 uptake, in another word, the CO_2 molecule coverage on carbon surface. At low CO_2 uptakes, that is, when CO_2 molecules just start to form monolayer coverage, they preferably adsorb on the active sites in the first place, such as nitrogen and metal dopants. This is reflected in Figure S3a that all samples except the acid-washed LC2-700H show observable higher heat of adsorption at the lower CO_2 uptake regime. In addition, Figure S3b shows LC2-600 has a much steeper curve before it reaches a plateaus, which suggests its heat of adsorption drops much faster than those of the other samples. This is attributed to the mixed contribution of both active and normal carbon sites to the heat of adsorption. The latter contributes less to the heat of adsorption, which lowers the overall heat of adsorption. After the formation of monolayer coverage, active sites may have much less influence on the second layer (or above) CO_2 molecules and thus the sample exhibits even lower heats of adsorption. Therefore, it explains the plateau region in Figure S3a and similarly 1st order derivative of HoA in Figure S3b for all the samples at higher CO_2 uptake region. Considering LC2-600 has both relatively higher levels of nitrogen and metal contents, compared with those of the other samples, it leads to high heats of adsorption at low CO_2 uptakes and the heat of adsorption drops steeply when the active sites is covered by CO_2 molecules.

Furthermore, Figure S3c integrates heat of adsorption from 0.1 to 8 wt% CO_2 uptake, which is an indication of overall effect of active sites throughout different levels of CO_2 uptakes. Figure S3c shows that the integrated heat of adsorption of all samples exhibits almost a linear relationship with CO_2 uptake. The positions of the linear plots in Figure S3c is in consistent with Figure S3a, where LC2-600 occupies the highest place. It indicates the positive influence of active sites on enhanced CO_2 binding across all levels of CO_2 uptakes.

5. Cyclic voltammetry

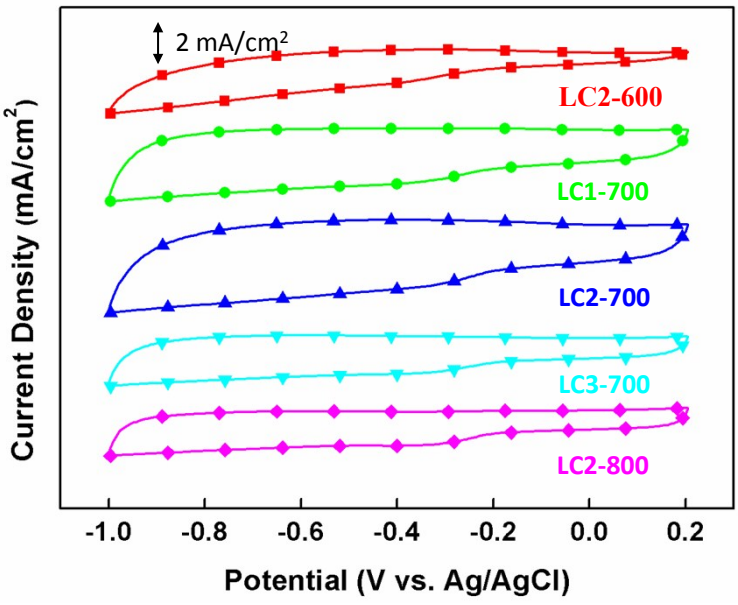

Figure S4 Cyclic voltammetry of LC-KOH samples.

6. Number of electron transfer

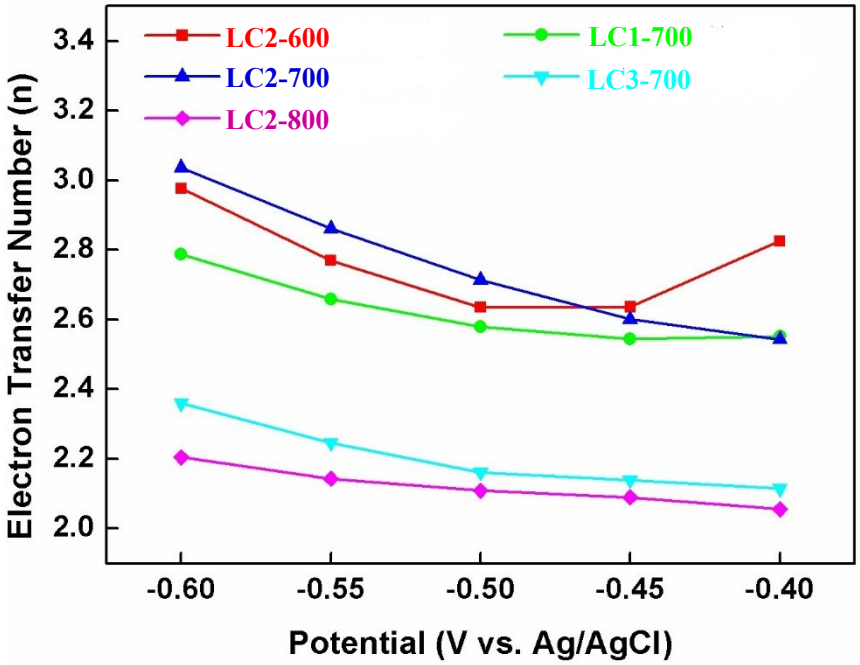

Figure S5 Number of electron transfer for KOH samples at the potential of -0.4 to -0.6 V vs. Ag/AgCl.

7. Elemental Mapping by TEM-EDX

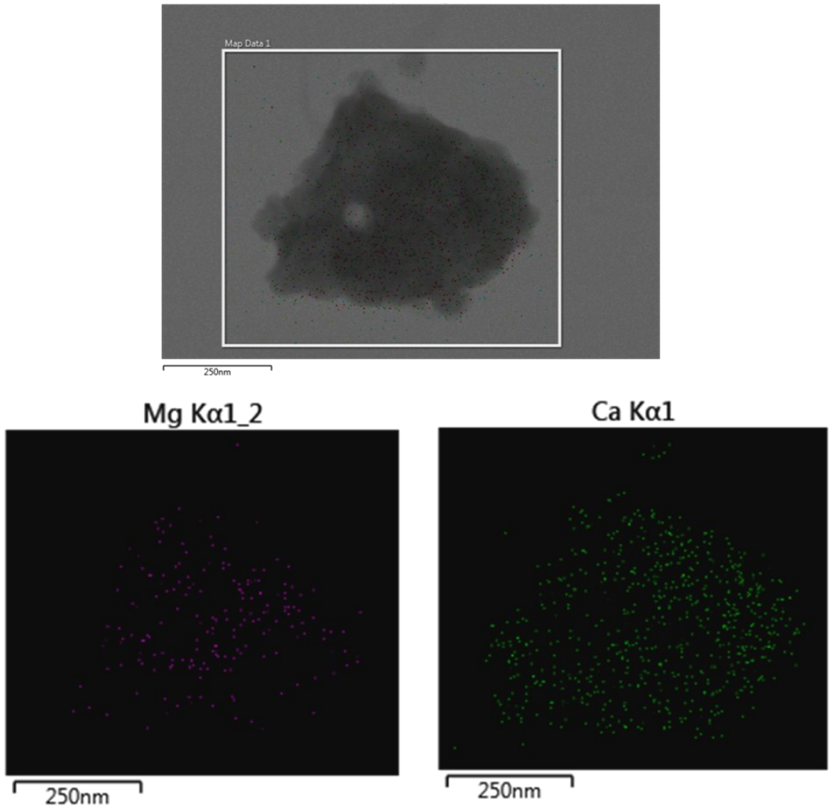

Figure S6: Elemental mapping by TEM-EDX shows uniform distribution of Mg and Ca in a piece of carbon sample.

8. CHN analysis

Table S2: Bulk chemical composition of leaf-derived carbon (unit: at%).

Sample	C	H	N	Other Elements
Leaf	52.12	6.67	2.21	39
LC0-600	72.58	2.23	2.18	23.01
LC2-600	57.21	2.55	1.17	39.07
LC2-700	58.44	2.64	1.02	37.9
LC2-800	60.3	1.89	0.1	37.71
LC1-700	60.25	1.71	0.66	37.38
LC3-700	51.22	2.59	0.14	46.05

The bulk chemical composition (rather than surface) of leaf and leaf-derived carbon was further analysed by a CHN elemental analyser (CE440, Exeter Analytical Ltd., UK). There are some differences between the results given by CHN and XPS analyses, indicating that nitrogen and metal elements are non-uniformly distributed in the surface and the bulk of the leaf and the leaf-derived carbon. Particularly, the nitrogen content detected by CHN in the leaf precursor is 2.21 at%, much higher than that detected by XPS (0.2 at%). The CHN analysis also shows there are large proportions of "other elements" in the leaf. This further supports the author's discussion on the detection depth limit of XPS as a surface chemistry characterisation technique, when it is used for biomass precursor characterisation. This also suggests nitrogen and metal elements are inherited from the biomass itself.

9. Carbon yield

Table S3: Carbon yield after carbonisation and activation (unit: wt%).

Carbonisation	
Leaf to LC0-600	33.3
Activation	
LC0-600 to LC2-600	79.7
LC0-600 to LC2-700	71.0
LC0-600 to LC2-800	61.7
LC0-600 to LC1-700	81.3
LC0-600 to LC3-700	64.7

It can clearly be concluded from Table S3 that the major weight loss is caused by the carbonisation process. When the carbonised leaf is activated by KOH, the carbon yield decreases with increasing KOH/carbon ratio and the activation temperature.